Supporting Information

Enzyme-Induced Dual-Network ε-Poly-L-lysine-Based Hydrogels with Robust Self-Healing and Antibacterial Performance

Rui Wang[1], Qing Li[1], Bo Chi[1], Xiaoqiao Wang[1], Zheng Xu[1], Zongqi Xu [1], Su Chen[1],and Hong Xu[1*]*

[1]State Key Laboratory of Materials-Oriented Chemical Engineering, Nanjing Tech University,

Nanjing 210009, P. R. China.

Content

1. Supporting Figures

1.1 FT-IR spectra of EPL-*g*-poly(NVP-*co*-NMA) hydrogels

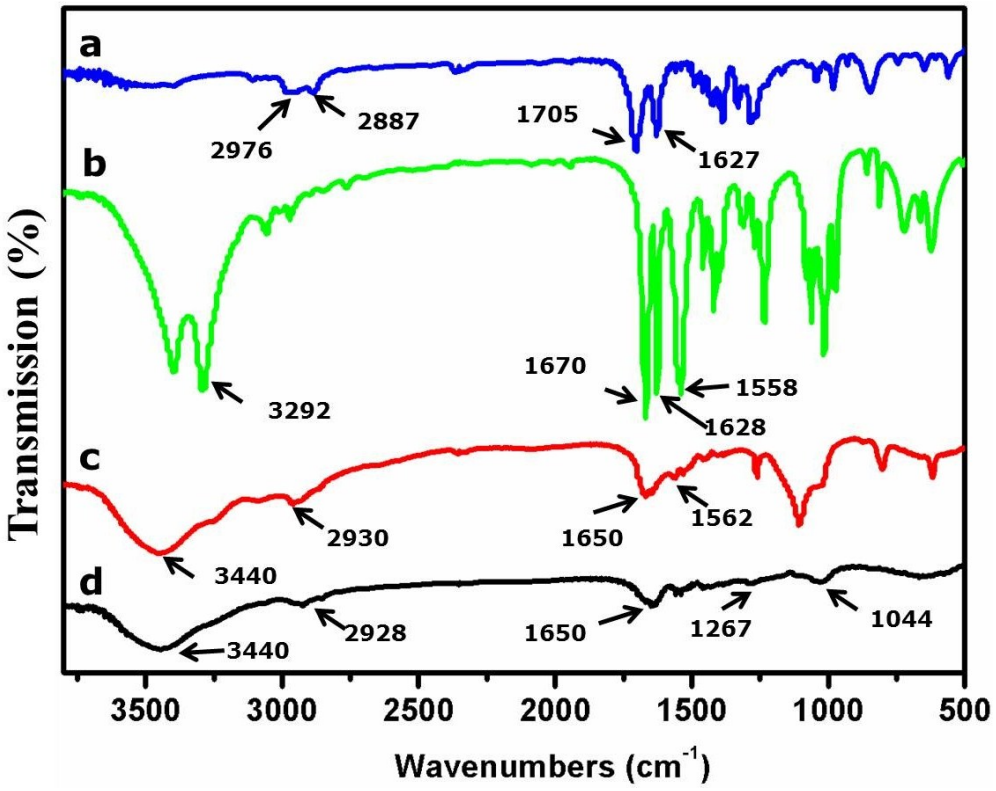

Supplementary Figure 1 | FTIR spectra of (a) NVP, (b) NMA, (c) EPL, and (d) EPL-*g*-poly(NVP-*co*-NMA).

To study the chemical structure of the obtained gels, fourier transform infrared (FTIR) spectroscopy were performed using Nicolet 6700 FT-IR spectrometer. The samples were immersed in water for several days at room temperature to remove the residual solvent and un-cross-linked monomers. During the immersion process, water was changed daily. After the moist hydrogels were dried in a vacuum oven at 60 °C till a constant weight. The dried samples of hydrogel, EPL powder, NVP powder, and NMA powder, were compressed into films with KBr for FT-IR measurement at a resolution of 4 cm^{-1} with 32 scans from 4000 to 500 cm^{-1}.

The FTIR spectra of the conjugates were compared with the corresponding initial NVP, NMA and EPL. In the spectrum of NVP, some characteristic absorption peaks can be ascribed at 2976 and 2887 cm^{-1} for asymmetric and symmetric aliphatic –C–H stretch, 1705 cm^{-1} for

C=O stretching vibration of cyclic amide, 1627 cm^{-1} for the C=C absorption, and 1044 cm^{-1} for C–C peaks on the NVP cyclic structure.[1] The NMA presents characteristic peaks at 3292 cm^{-1} belonging to the stretch vibration of $–NH_2$ group, at 1670 cm^{-1} reflecting the stretching vibration of C=O group, at 1628 cm^{-1} assigned to the bending vibration of N-H group or C=C absorption.[1] In the case of of EPL, the characteristic bands are found at 3440 cm^{-1} (NH_2 asymmetric stretching vibration), 2930 cm^{-1} (C-H stretching vibration), 1562 cm^{-1} (NH bending, amide II), 1650 cm^{-1} (carbonyl group stretching vibration, amide I), and 1245 cm^{-1} (C–N stretching of amide bands).[2, 3] The new absorption band at 2928 cm^{-1} was observed, attributed to –C–H stretching band, which indicates that the monomers are successfully polymerized and crosslinked by breaking the C=C bond. In addition, the absorption peaks at 3440 cm^{-1} originating from the NH_2 stretching of EPL were still detected in the hydrogel. This finding indicates the presence of excess free amino groups. These free amino groups provide the possibility for further enzyme catalysis and antibacterial application.

1.2 Preparation of EDHs

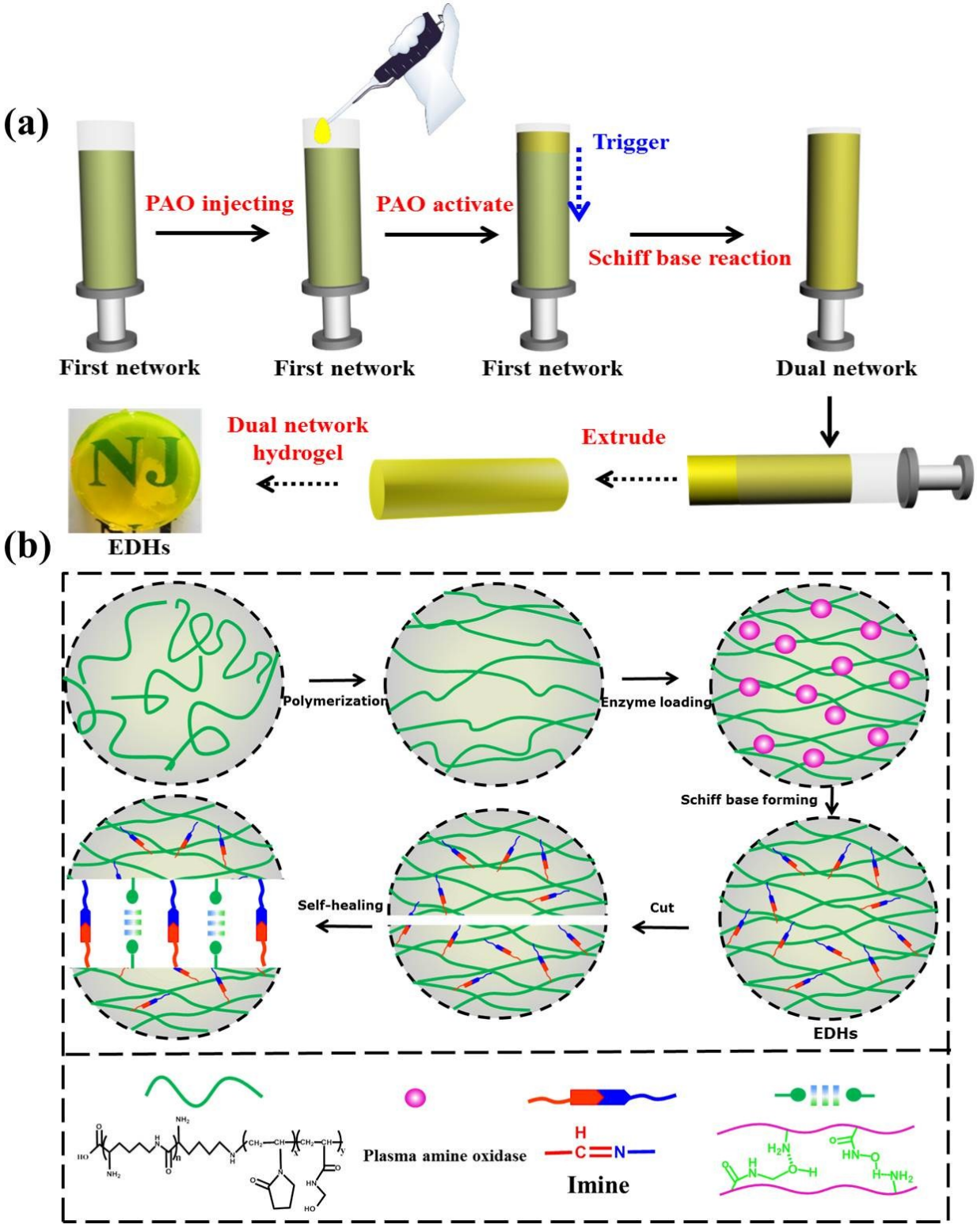

Supplementary Figure 2 | Schematics of preparation of EDHs and the mechanism of self-healing. (a) Preparation of EDHs. (b) The mechanism of self-healing in EDHs.

In this work, the EDHs were first prepared by free radical polymerization (FRP) of EPL, NVP and NMA in water at room temperature. NVP is one type of materials with high viscidity and good biocompatibility, which has been widely employed in biomedical field.[4] However, the poor mechanical strength limited its potential application. To address this issue, NMA was chosen as the copolymerization monomer in the hydrogel network. Additionally, EPL, as a bioadhesive, has been exploited in wound healing because of its excellent biocompatibility and antibacterial properties.[5-7]

The monomers were in situ polymerization to form first chemically crosslinked network, the second crosslinked network was formed after 150 μl plasma amine oxidase (PAO) loading (30 U ml^{-1} of stock solution) and re-organization of coordinates. The strong bonds (dynamic schiff base linkage) serve as permanent crosslinking points, and the weak bonds (intrinsic hydrogen bonds interaction) act as sacrifical bonds that rupture under deformation.

1.3. Scanning electron microscopy (SEM) characterization of EDHs

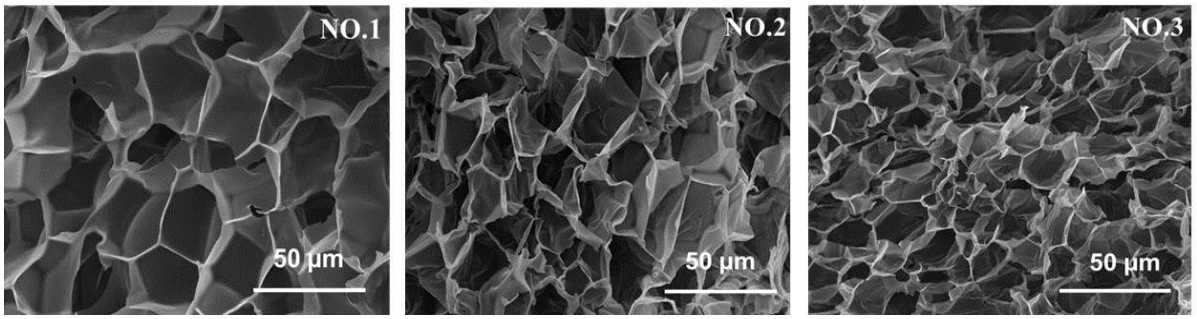

Supplementary Figure 3 | SEM images of EDHs. EDHs are fabricated with EPL/monomer = 4% (wt/wt), BIS = 0.01 wt% at different [NVP]/[NMA] mass ratios of (a) 5/1 for No.1, (b) 5/2 for No.2 and (c) 5/3 for No.3.

The microstructures of the hydrogels were examined by SEM with a QUANTA 200 (Philips-FEI, Holland) at an acceleration voltage 20.0 kV. The samples were purified by immersing in deionized water for 5 days to remove any water-soluble materials. Then the samples were freeze-dried for 24 h. After that, frozen samples were plunged into a liquid nitrogen bath, and were cut to expose their inner structure. For SEM measurement, the slices of samples were sputter coated with a thin layer of platinum metals prior to imaging.

It is noted that all of the hydrogels exhibit an interconnected and porous three-dimensional structure. Moreover, the three discriminative SEM images suggests that the cross-section structure of the hydrogel network is dependent on the hydrogel composition. With an increase in the ratio of NVP/NMA from 5/1 to 5/3 (**Supplementary Table 1**), the porosity size of the hydrogels structure tended to be more uniform and intact. These results may be directly correlated with the comparatively sufficient crosslinking of hydrogel architecture.

Supplementary Table 1 | Different ratio of NVP/NMA of EDHs for SEM and mechanical properties studies

Sample No.	NVP/NMA(g/g)	BIS(wt.%)	EPL(wt.%)
NO.1	5 : 1	0.02	0.1
NO.2	5 : 2	0.02	0.1
NO.3	5 : 3	0.02	0.1

1.4. Rheological properties of EDHs

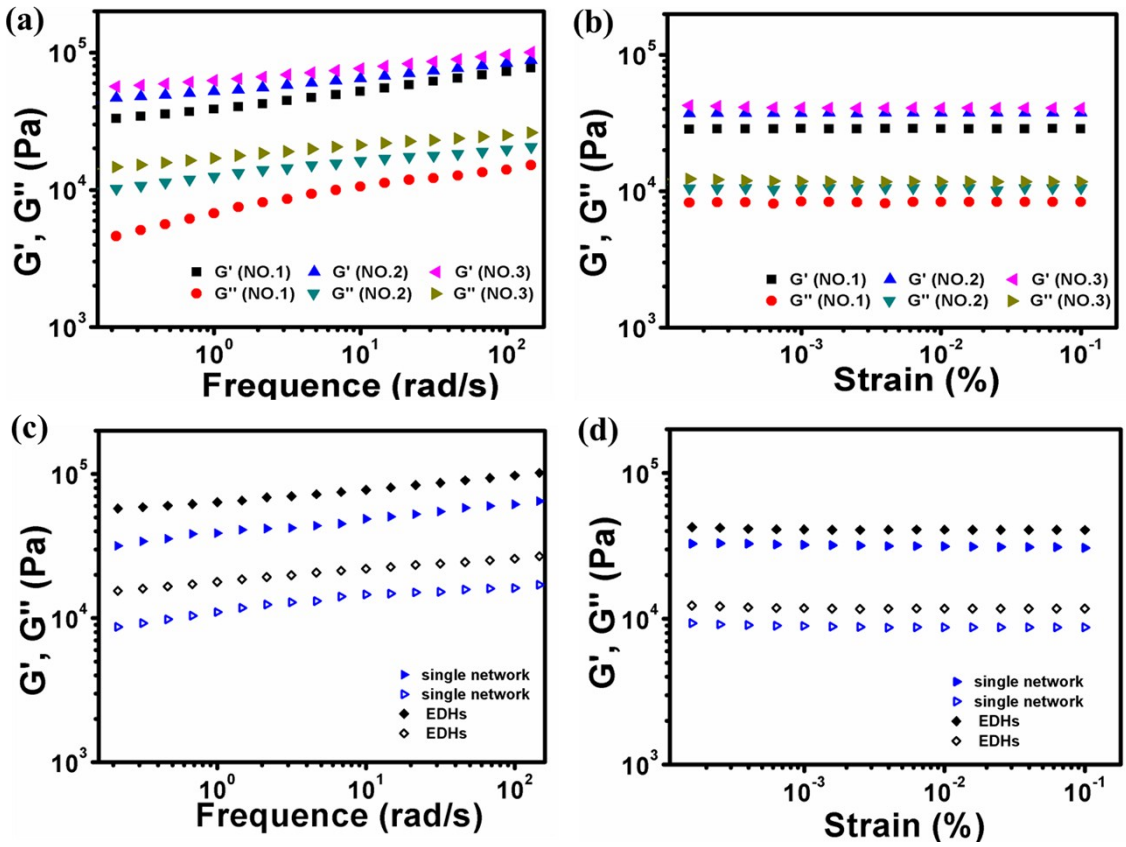

Supplementary Figure 4 | Mechanical properties of EDHs. Storage modulus (G′) and loss modulus (G″) values of EDHs on (a) frequency sweeps, (b) strain sweeps with EPL/monomer=4% (w/w), BIS=0.01 wt% at different [NVP]/[NMA] mass ratios of 5/1 for No.1, 5/2 for No.2 and 5/3 for No.3, and (c, d) rheological parameters of the single network EPL-g-poly(NVP-co-NMA) hydrogels before and after the treatment of enzyme.

Rheological characterizations of the EDHs were performed using a HAAKE RheoStress 600 instrument with a parallel plate of 20 mm diameter. All tests were conducted at 25 °C. Subsequently, the storage modulus (G′), loss modulus (G″) value were recorded as a function of frequency and strain, respectively. G′ corresponds to the elastic property of the hydrogel, whereas G″ represents the viscous property. Note that all of the hydrogels display an elastic characteristic with G′ higher than G″. This is a typical behavior of polymer hydrogels. Furthermore, the mechanical strength increased along with the rising content of NMA in the

hydrogel composition. The reinforcement in mechanical strength might result from the comparatively sufficient crosslinking of hydrogel network, which is in accordance with the morphology results. The rheological parameters of the single network EPL-g-poly(NVP-co-NMA) hydrogels before and after the treatment of enzyme were investigated: EPL/monomer=4% (w/w), BIS=0.01 wt% , [NVP]/[NMA] = 5/3 (mass ratios)

1.5. Self-healing performance of the EDHs

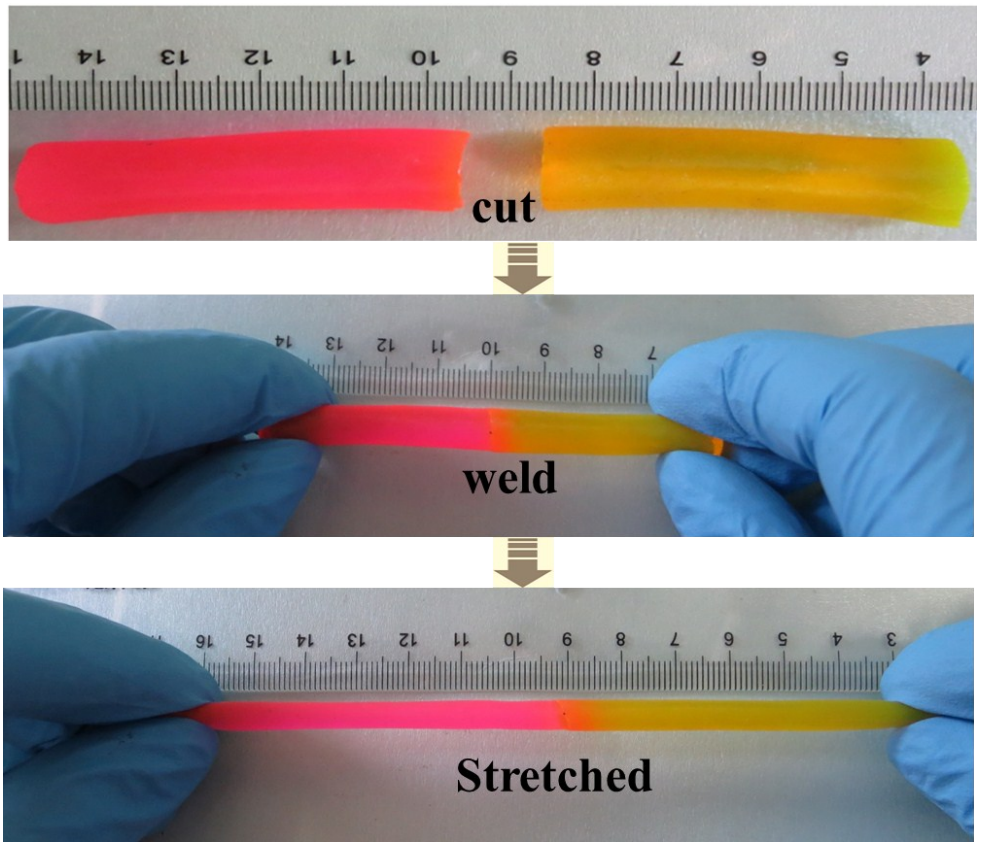

Supplementary Figure 5 | Self-healing performance of the EDHs. Two hydrogel blocks were attached together, after that the fractured surfaces kept for 24 h at room temperature without any other intervention, and then the cracks were successfully cured.

1.6. IR images of the healing process of control hydrogels.

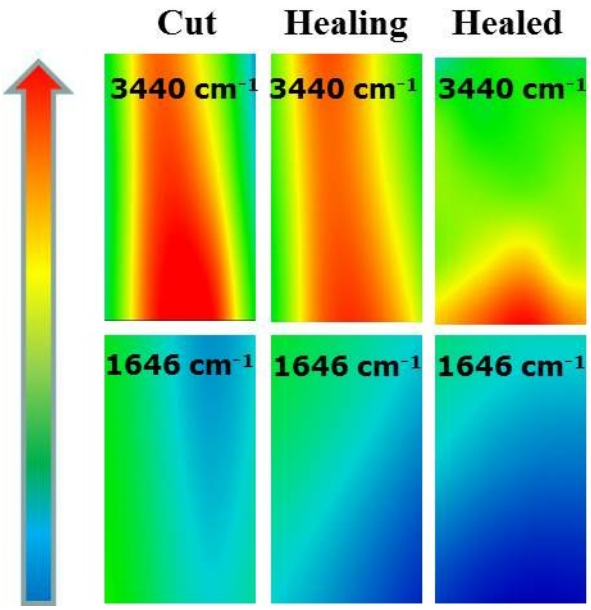

Supplementary Figure 6 | (a) Cutting edge; (b) Healing interface; (c) Healed interface of EPL-*g*-poly(NVP-*co*-NMA) hydrogels.

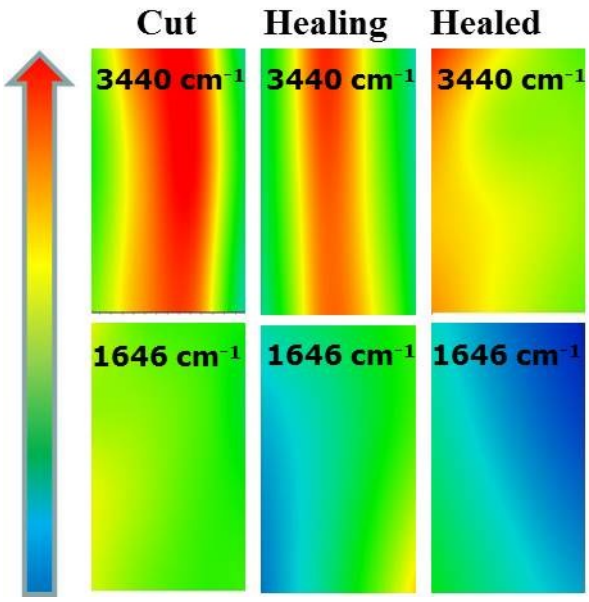

Supplementary Figure 7 | (a) Cutting edge; (b) Healing interface; (c) Healed interface of EPL-*g*-poly(NVP-*co*-NMA) hydrogels treated with PBS.

1.7. 3D IR images of the healed process of EDHs

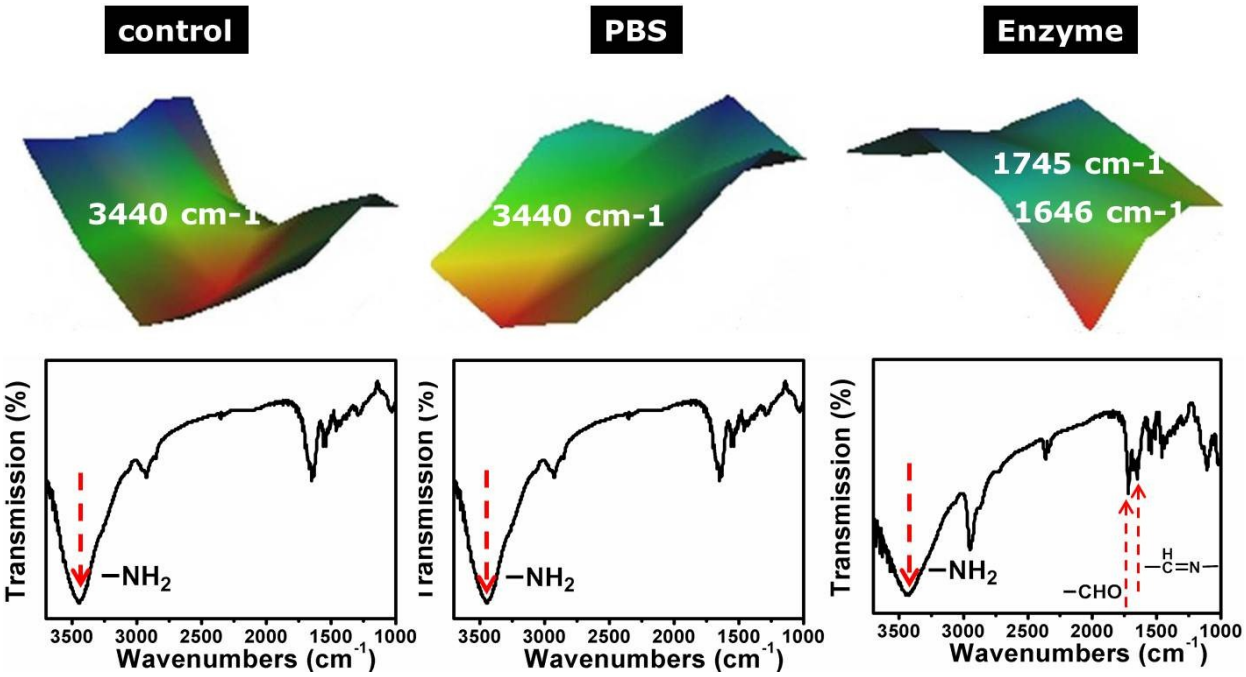

Supplementary Figure 8 | 3D IR images of the healed area of EPL-*g*-poly(NVP-*co*-NMA) hydrogels (control), the sample treated with PBS, and EDHs, respectively.

1.8. Mechanism of the enzymatic reaction mediated by plasma amine oxidase.

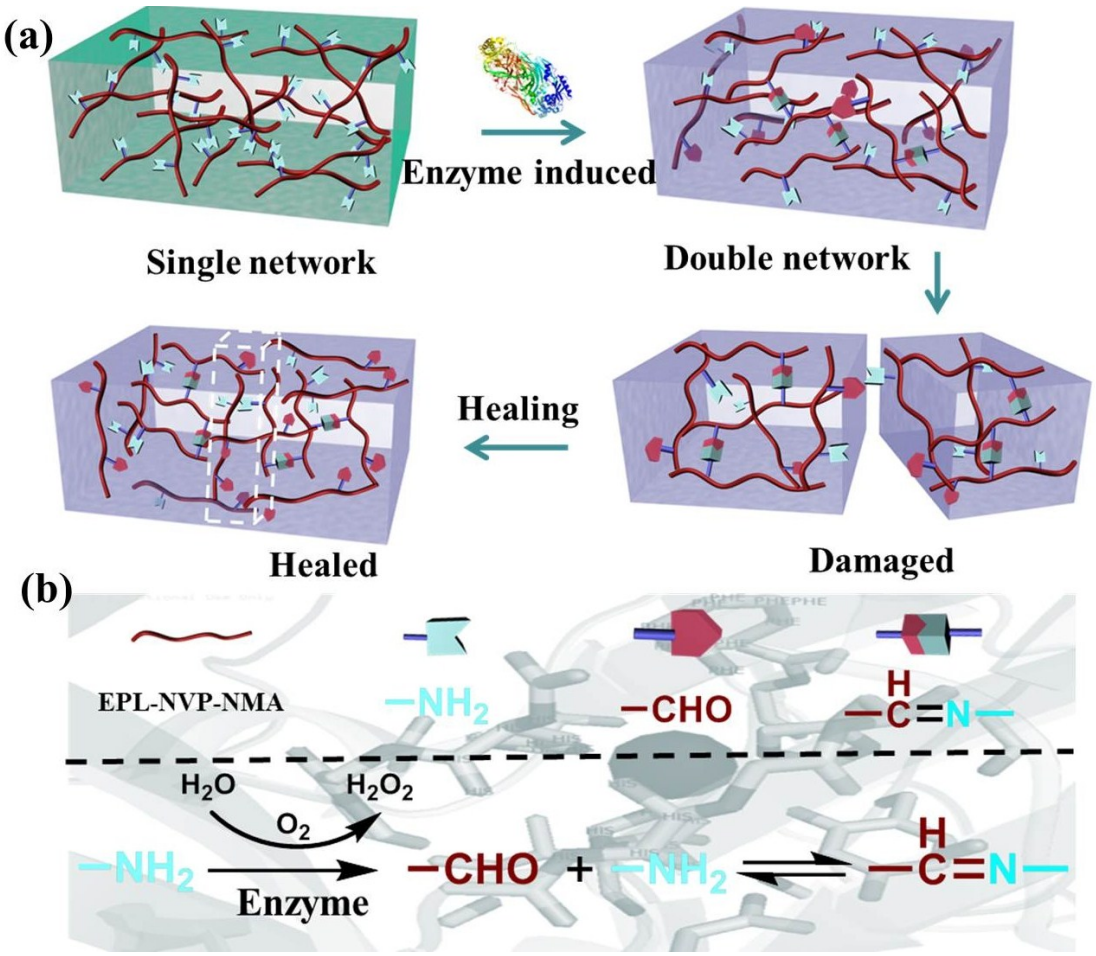

Supplementary Figure 9 |(a) Schematic illustration of enzyme-induced self-healing hydrogel; (b) mechanism of the enzymatic reaction mediated by plasma amine oxidase.

1.9. Enzyme-mediated self-healing mechanism of EDHs at molecular level

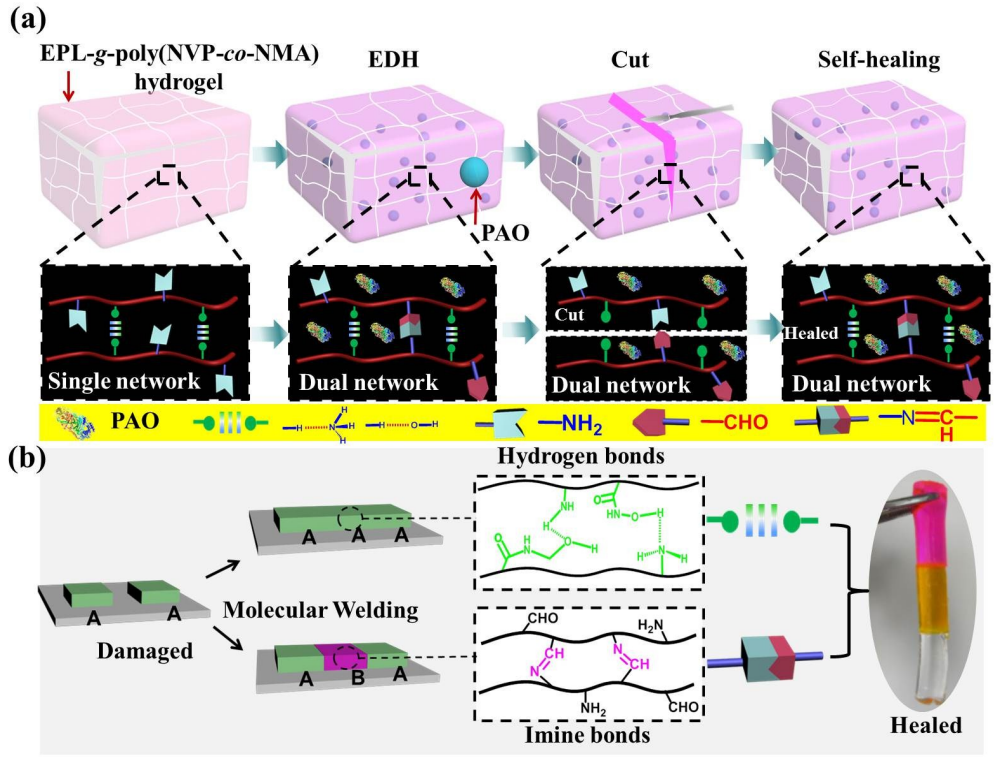

Supplementary Figure 10 | Schematic illustration of enzyme-regulating self-healing in dual-network hydrogel EDHs. (a) Demonstration of the enzyme-induced Schiff base reaction to construct dual-network self-healing hydrogel and auto-healing process based on dynamic Schiff base linkage. (b) Molecular welding mechanism of self-healing arising from the imine bonds and hydrogen bonds.

The intriguing enzyme-mediated self-healing mechanism can be explained at molecular level. The starting hydrogel network is firstly built by free radical polymerization of EPL, NVP, and NMA. Then the PAO activates the Schiff base reaction in the first network and hence dual-network hydrogels are achieved. The polymer chains of the single-network hydrogel just provide intermolecular hydrogen-bonding force between amino groups (NH_2) in EPL and hydroxy groups (OH) in NMA chain. The noncovalent hydrogen bonds, serving as the soft phase and providing toughness, are crucial for self-healing. However, after the introduction of PAO, a new enzyme-induced Schiff base reaction occurs in situ to generate dynamic covalent imine structure (−CH=N−) as the secondary crosslinking network in this

case. These dynamic covalent bonds can provide hard phase and reversible interaction to increase the modulus and toughness. In this dual-network system, the fracture and regeneration of internal hydrogen bonds and the dynamic imine bonds can continuously proceed to homogenize the network, allowing their molecules to be weld rapidly, thereby endowing the superior self-recovery capability (95%) of the EDHs. This result gives a new and green approach for building synthetic material with effective self-healing capacity.

2.0. In vitro antibacterial study of EDHs

Supplementary Table 2｜ MIC (μg/mL) of of EPL and EDHs

.Test organisms	MIC ($\mu g/ml^{-1}$)	
	EPL	EDHs
E. coli	12	18
S. aureus	19	23

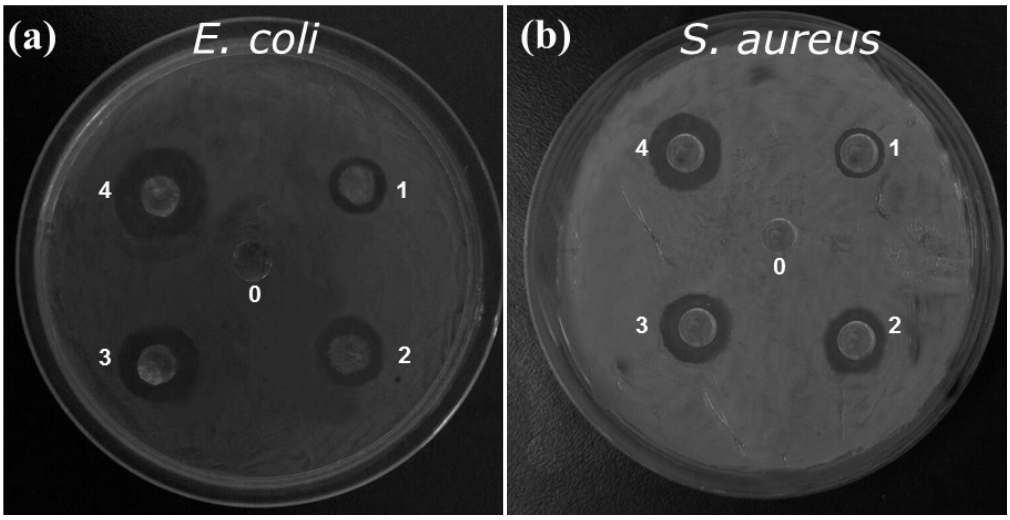

Supplementary Figure 11 ｜Inhibition zone tests of EDHs with different EPL/monomer (w/w) against (a) *E. coli* and (b) *S. aureus*: (0) EPL/monomer=0%; (1) EPL/monomer=1%; (2) EPL/monomer=2%; and (3) EPL/monomer=3%. (4)EPL/monomer=4%.

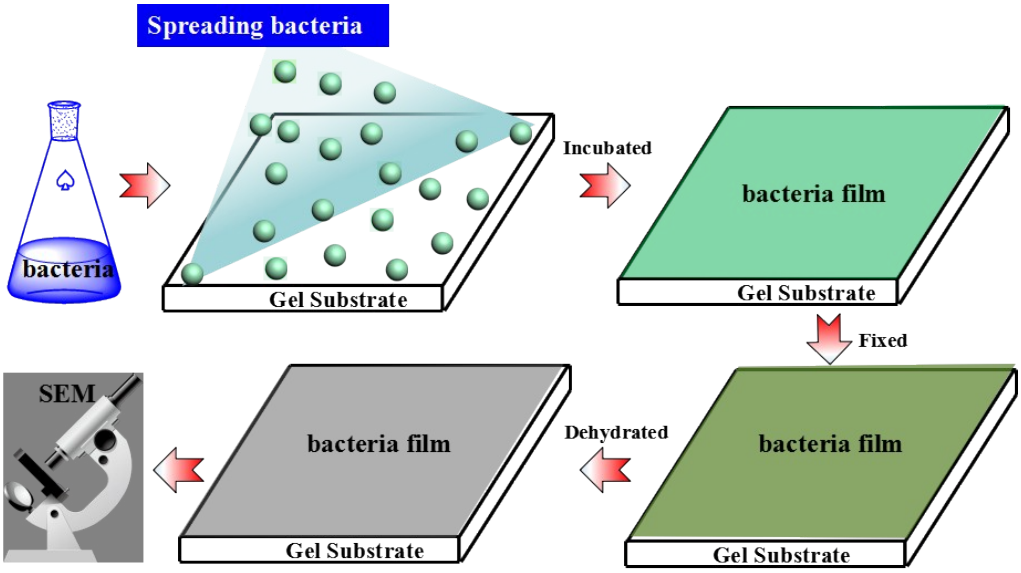

Supplementary Figure 12 | Schematic illustration of the microbes seeding and fixing on the hydrogel films.

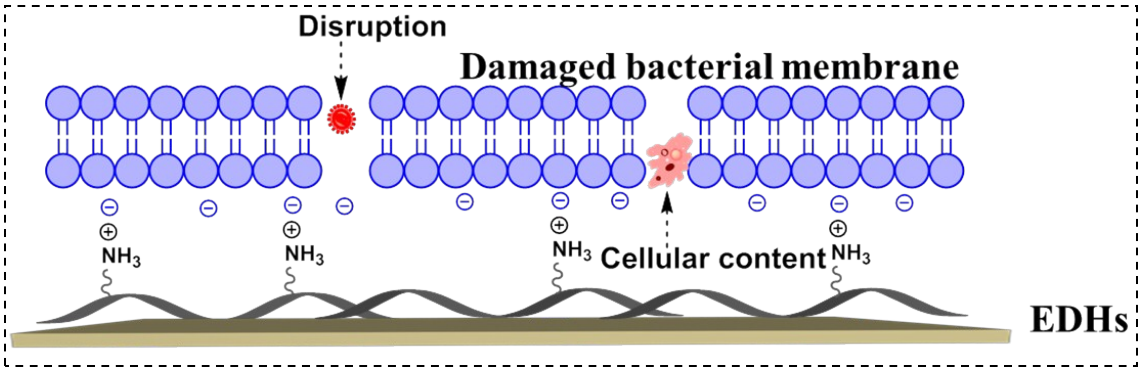

Supplementary Figure 13 | Schematic diagram of the interaction mechanism between EDHs and the bacterial membranes.

For the microorganism morphology study, 10 μL inoculum of each pathogen was sprayed on 2 × 2 cm EDHs and LB agar gel (control) surface and incubated at 37 °C for 2 h. Then the bacteria were fixed with glutaraldehyde (2.5%) for 4 h, after which the gel plate were dehydrated using an ethanol series (20-100%; 15-30 min), and subsequently freeze-dried. The dried hydrogels films were characterized using Scanning Electron Microscopy (Philips-FEI, Holland) for microbe morphology change.

Minimum inhibitory concentrations (MICs). Firstly, a two-fold dilution series of 100 μl polymers (EPL and EDHs) solution was prepared and added to a 96-well tissue culture polystyrene (TCPS) plate. Then 100 μL bacterial suspension in LB solution was added to each well to achieve a final concentration of 10^5 CFU/mL. After that, the 96-well plate was incubated at 37 °C for 18 h. The MIC was taken at the lowest material's concentration at which completed inhibition to bacterial cell growth. The solution without polymers and without broths were used as the positive control and negative control, respectively. The test was repeated three times for each sample.

Inhibition zone tests. The inhibitory effect of hydrogels on bacteria was further determined by the inhibition zone tests. Briefly, a series of EDHs disks (0.5 cm in diameter) with different amount of EPL (1 wt.%, 2 wt.%, 3 wt.%, 4 wt.%) were prepared and named as 1, 2, 3, 4, respectively. The hydrogel without EPL was used as the control, which was defined as 0. Subsequently, the hydrogels samples were covered on the LB petri dishes containing bacteria (*E. coli* and *S. Aureus*). Antibacterial activity was evaluated by the circular clear zones on the opaque background of bacterial growth after incubation at 37 °C for 24 h, which defined as the ability of the hydrogel to inhibit bacterial growth.

2.1. In vitro biocompatibility study of EDHs

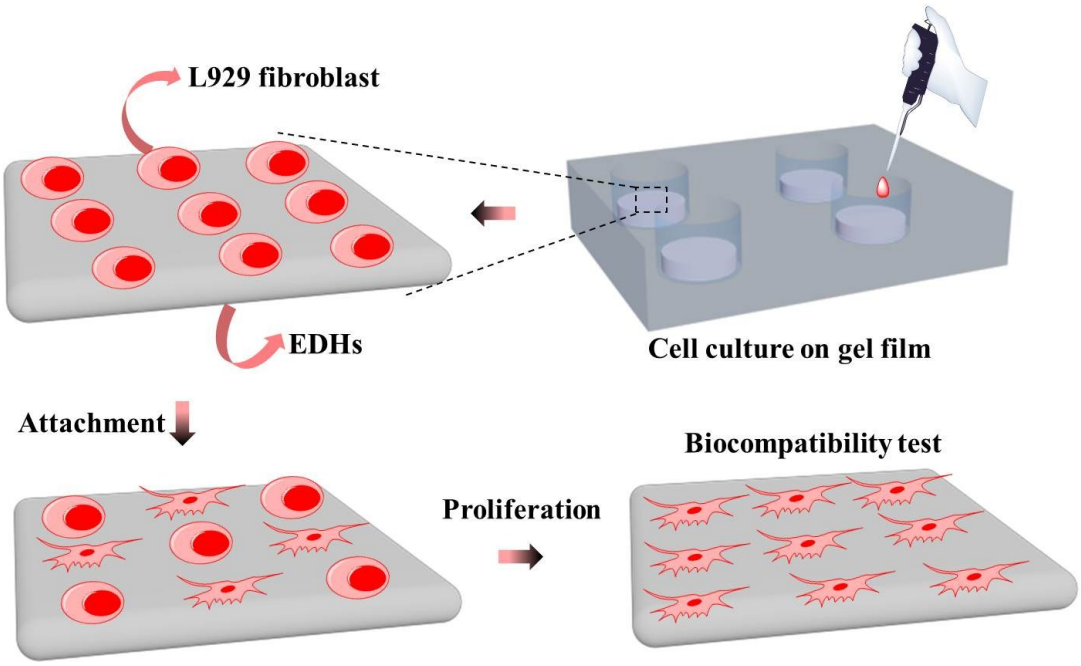

Supplementary Figure 14 |Schematic illustration of L929 fibroblast seeding on the hydrogel films and biocompatibility studies.

In vitro biocompatibility studies. Cell viability were evaluated with MTT assay and Live/Dead assay. For the study, L929 fibroblast were cultured with the hydrogel matrices in vitro for 3 days, with normal culture plate as a control. For the cell culture experiments, the L929 mouse fibroblast at passage 3 were used with non-differentiation culture medium (DMEM containing 10% FBS, 1% penicillin/streptomycin). Before cell seeding, the EDHs films were pretreated and sterilized following the method described above. Cells and moderate culture medium were added to the 96-well culture plates. The density of the cells was 1×10^5 cells/mL. After cells were incubating into the plate for about 4-5 h, the hydrogel samples were introduced into the wells. Subsequently, the cells was cultured with the hydrogel matrices for various periods under standard cell culture conditions (37 ℃ and 5% CO_2). As a control, cells were incubated in tissue culture polystyrene dish (TCPS) wells without hydrogels under the same condition. After specified culture periods, MTT reagent (thiazolyl blue tetrazolium bromide; Sigma, USA) was added to each well of the 96-well plates and incubating for 4 h at 37 °C. Then DMSO (200 μL) was added into the plate. After

incubating for 30 min, the colorimetric measurements were performed at 490 nm using a 96-well microplate reader (Biorad). Data were expressed as mean ± standard error of mean of at least five independent experiments. In additon, for the LIVE/DEAD assay, the hydrogels were taken out and transferred into a new 96-well TCPS plate. Live/Dead assay reagents containing 2 mM calcein AM (labeled live cells) and 4 mM EthD-1 (labeled dead cells) were added, and then the plate was kept in an incubator in the dark at room temperature for 30 min. After solution removal and PBS rinsing, the morphology of fluorescently labeled cells was visualized by laser scanning confocal microscopy (Leica TCS SP5).

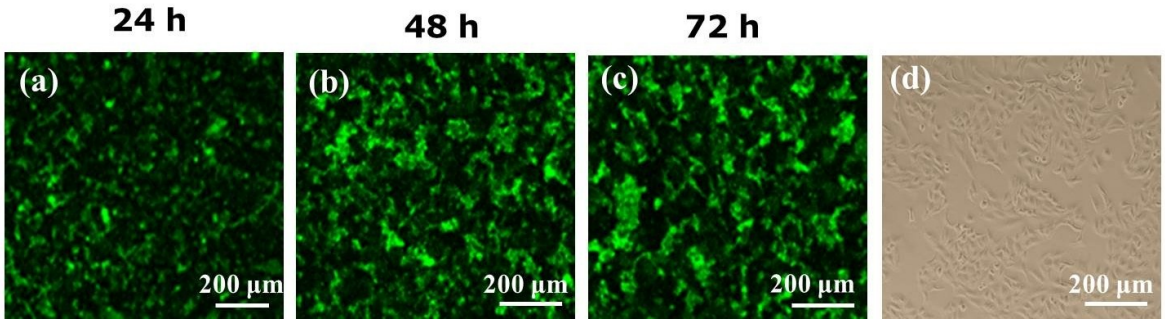

Supplementary Figure 15 | In vitro biocompatibility of EDHs. (a) LIVE/DEAD cell assay of L929 fibroblast after cultivating on EDHs for 24, 48, and 72 h, respectively. (b) Optical images of L929 fibroblast cultivating on EDHs at 72 h. The seeding density is 1×10^5 cells/cm^2.

2.2. Histologic, immunohistochemical analysis

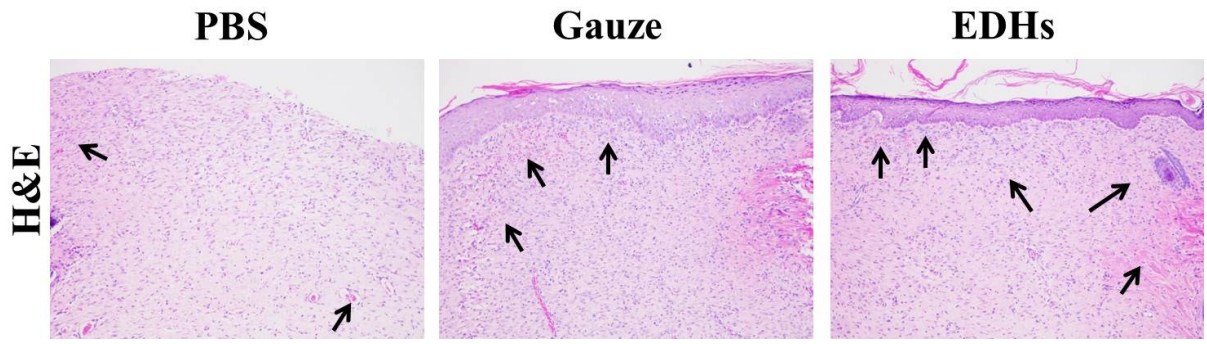

Supplementary Figure 16｜Representative images of H&E stained histological sections on 14 days after transplantation. Black arrow indicate newly formed blood vessels with their typical round or oval structure. Scale bars indicate 400 μm. Mean ± SD; n = 6.

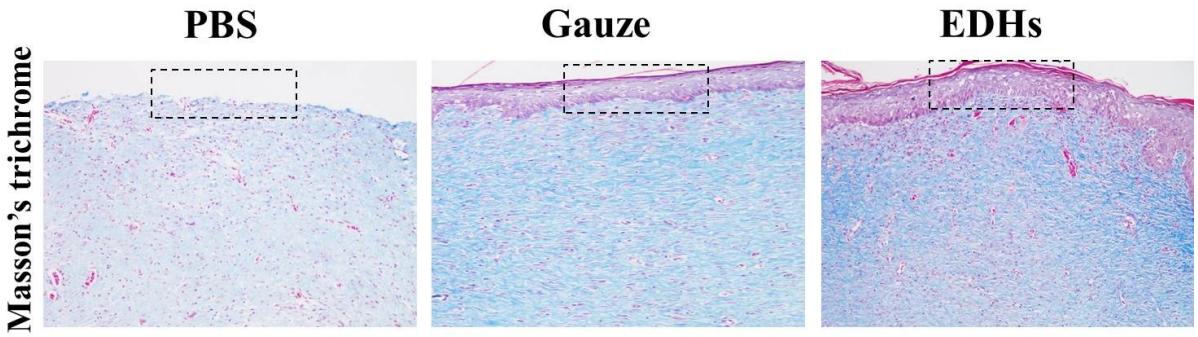

Supplementary Figure 17 | Representative images of Masson's Trichrome stained histological sections on 14 days after transplantation. Dotted box indicate wavy collagen fibers. Scale bars indicate 400 μm. Mean ± SD; n = 6.

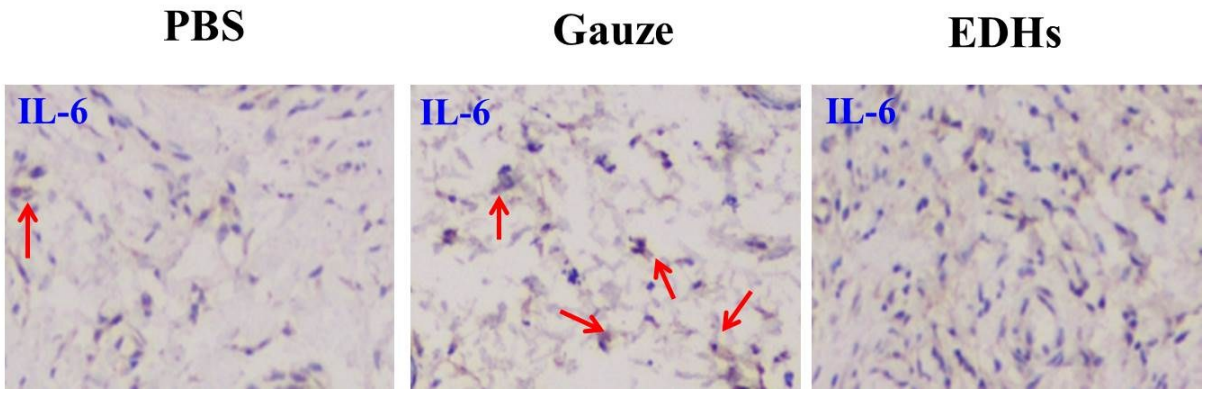

Supplementary Figure 18 | Immunohistochemical staining for IL-6 stained sections of the PBS, Gauze or EDHs treated defects at 14 days post-surgery. Scale bars indicate 400 μm.

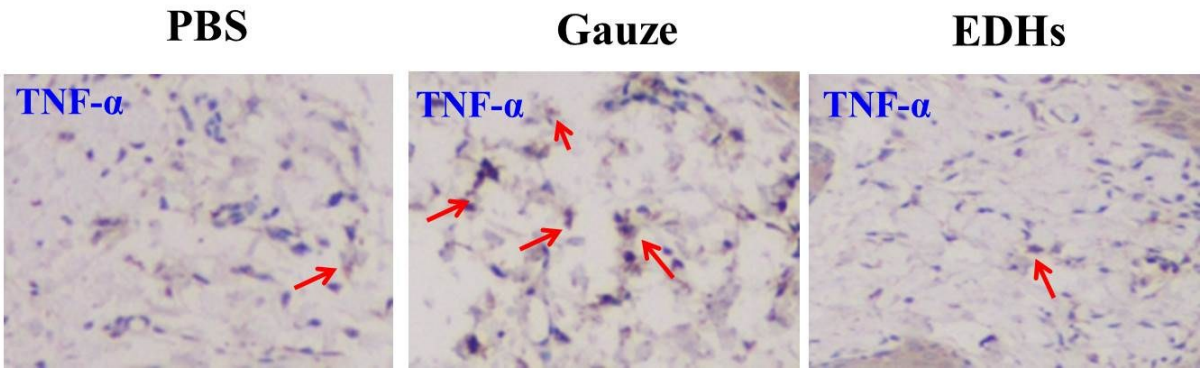

Supplementary Figure 19｜Immunohistochemical staining for TNF-α stained sections of the PBS, Gauze or EDHs treated defects at 14 days post-surgery. Scale bars indicate 400 μm.

Animal experiment for wound closure. The biocompatibility in vivo and wound healing efficacy of the EDHs were evaluated using 15 healthy male Sprague-Dawley rats (180–250 g, Jinling Hospital, Nanjing, China). All the animal care and experimental protocols were approved by Animal Investigation Ethics Committee of Jinling Hospital. The rats were randomly divided into three groups and each group contains five rats (n = 5). Prior to surgery, the rats were anaesthetized by intraperitoneal injections of a ketamine (50 mg/kg body weight) and xylazine (5 mg/kg body weight) mixture. Dorsal hair of each rat was shaved and a full-thickness skin wounds (diameter = 1.0 cm) were created on each sides of the rat's back under aseptic conditions. The incisions were filled with PBS (control), gauze and EDHs, respectively. After which the dressing materials were fixed with plastic sheet, and the rats were individually housed in cages with a standard diet under normal room temperature. On day 0, 3, 7 and 14 post-surgery, the wounds were photographed using a digital camera (Canon, Japan). The wound closure rate was assessed by analyzing the planimetric digital images according to the following equation:

$$\text{Percent wound size reduction} = [(A_0 - A_t)/A_0] \times 100 \quad (1)$$

where A_0 is the initial wound area (t = 0) and A_t is the wound area at designated time point.

Histologic, immunohistochemical analysis. The rats were sacrificed at 14 days post-surgery and the skin wound tissue of the rat was excised. The specimens were fixed in 10% formalin, dehydrated with a graded series of ethanol and embedded in paraffin. Representative sections were stained using hematoxylin−eosin (H&E) and masson's trichrome staining for histological observations. Images were acquired using an optical microscope. Besides, immunohistochemical staining of the specimens was performed to assess inflammatory reactions during the wound healing process by examining the protein level of IL-6 and TNF-α. After treatment，the tissue sections were first incubated with the rabbit anti-active IL-6 and rabbit anti-active TNF-α antibody (primary antibodies,1:200,

Proteintech), then they were incubated with goat anti-rabbit (the secondary antibodies, 1:200, Enogene Biotech. Co.,Ltd). All images were captured with the help of a fluorescent microscope (Model XSP-C204).

It is noted from the H&E staining that an enhanced number of new blood vessels are observed in the EDH-treated wound compared with the PBS and gauze groups (Fig. S16, ESI†). The greater formation of blood vessels contributes to the acceleration of granulation tissue formation in the wound bed. In addition, Masson's trichrome staining (Fig. S17, ESI†) showed that a more extensive collagen deposition was observed in the skin defects treated with the EDHs as compared to the defects treated with the control groups, reflecting the positive effect of the EDHs on the dermis tissue reconstruction at the wound sites. Moreover, the immunohistochemical analysis of tissue obtained from the gauze-treated rats exhibited higher a density of positive staining for both IL-6 and TNF-a (Fig. S18 and S19, ESI†). IL-6 and TNF-a are commonly used to evaluate inflammatory reactions or foreign body responses, which were primarily localized in the cytoplasm.[8] In contrast, few significant positive staining results for these inflammatory cytokines were observed for the EDH group. This indicated that the wound showed a minimal inflammatory response to the EDHs. These results might be due to the moist environment provided by hydrogels, which are able to stimulate wound healing. The moist EDHs are able to not only absorb exudate but also prevent water evaporation and wound dehydration,[9–12] suggesting an ideal environment to accelerate the wound healing (Fig. S20, ESI†). Additionally, the excellent in vivo biocompatibility is attributed to hydrogels' superior antimicrobial ability and good in vitro biocompatibility.

2.3. The mechanism of EDHs accelerating the wound healing

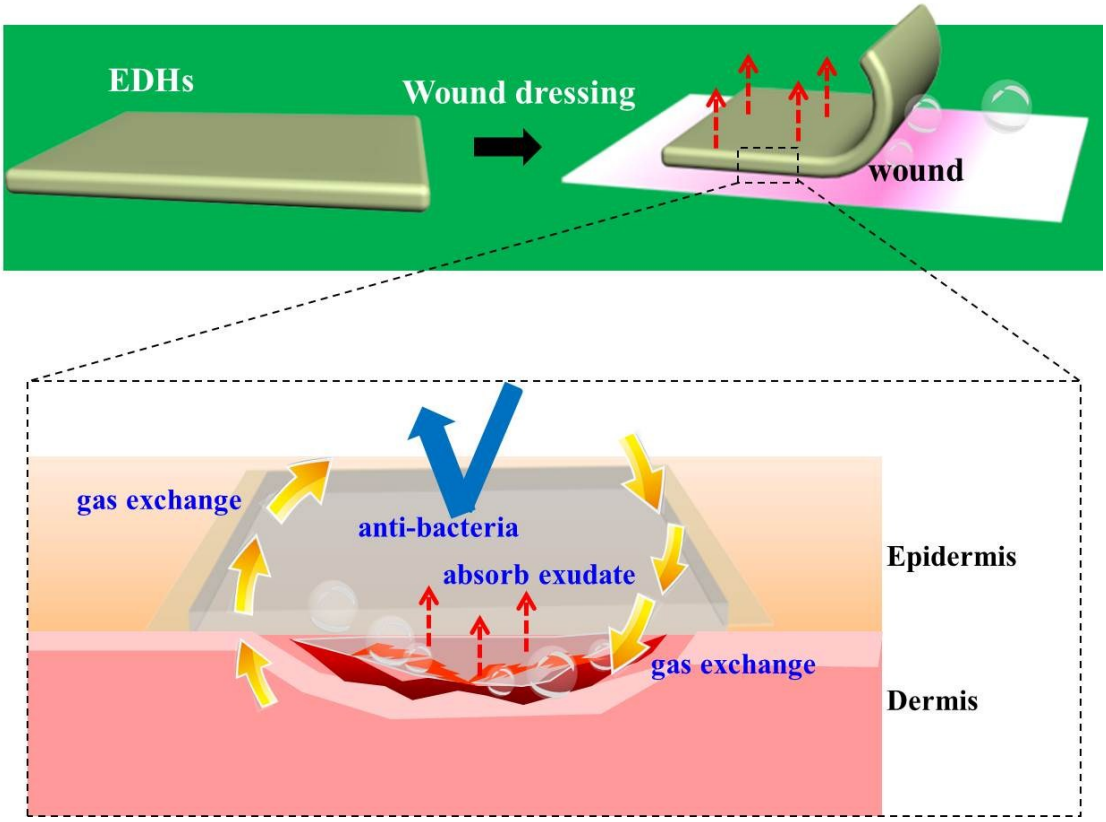

Supplementary Figure 20 | Schematic illustration of EDHs accelerating wound healing as wound dressing.

References

1. N. Nakajima, H. Sugai, S. Tsutsumi and S. H. Hyon, *Key Eng Mater*, 2007, **342**, 713-716.

2. L. M. Zhang, R. C. Li, F. Dong, A. Y. Tian, Z. J. Li and Y. J. Dai, *Food Chem.*, 2015, **166**, 107-114.

3. J. Chen, M. Liu, H. Liu and L. Ma, *Materials Science and Engineering: C*, 2009, **29**, 2116-2123.

4. C. X. Liang, F. Yuan, F. G. Liu, Y. Y. Wang and Y. X. Gao, *Int. J. Biol. Macromol.*, 2014, **70**, 427-434.

5. W. Nie, X. Y. Yuan, J. Zhao, Y. L. Zhou and H. J. Bao, *Carbohyd. Polym.*, 2013, **96**, 342-348.

6. R. Wang, B. Zhou, W. Liu, X. H. Feng, S. Li, D. F. Yu, J. C. Chang, B. Chi and H. Xu, *J. Biomater. Appl.*, 2014, **29**, 1167-1179.

7. Y. Fang, C. F. Wang, Z. H. Zhang, H. Shao and S. Chen, *Sci. Rep.-UK*, 2013, **3**, 2811.

8. V. Ballotta, A. I. P. M. Smits, A. Driessen-Mol, C. V. C. Bouten and F. P. T. Baaijens, *Biomaterials*, 2014, 35, 9100–9113.

9. F. Unger, M. Wittmar and T. Kissel, *Biomaterials*, 2007, 28, 1610–1619.

10. D. Okan, K. Woo, E. A. Ayello and G. Sibbald, *Adv. Skin Wound Care*, 2007, 20, 39–53.

11. N. Q. Tran, Y. K. Joung, E. Lih and K. D. Park, *Biomacromolecules*, 2011, 12, 2872–2880.

12. B. Balakrishnan, M. Mohanty, A. C. Fernandez, P. V. Mohanan and A. Jayakrishnan, *Biomaterials*, 2006, 27, 1355–1361.